Materials International
Open-Access Journal (ISSN: 2668-5728)

Article
Volume 7, Issue 3, 2025, 30
https://doi.org/10.33263/Materials73.030

Mg, Zn, and CO_3 Multi-Substituted Hydroxyapatite Nanopowders: Synthesis, Characterization, Cytotoxicity, and Antimicrobial *in vitro* Study

Sara Korowash [1,*], Hanan Abo-Almaged [1], Hossam El-Masry [2], Doreya Ibrahim [1]

[1] Refractories, Ceramics and Building Materials Department, National Research Center, 12622 Dokki, Cairo, Egypt; sara_ibrahim_science@yahoo.com (S.K.); hanan-202@hotmail.com (H.A.); doreya.ibrahim@yahoo.com (D.I.);
[2] Chemistry of Natural and Microbial Products Department, National Research Center, 12622 Dokki, Cairo, Egypt; drhossamnrc33@gmail.com;
* Correspondence: sara_ibrahim_science@yahoo.com;

Received: 15.01.2025; Accepted: 27.07.2025; Published: 10.09.2025

Abstract: This research focuses on developing multi-substituted hydroxyapatite (HA) nanopowders with enhanced antimicrobial properties and biocompatibility. Through a wet precipitation process, magnesium (Mg) and zinc (Zn) ions were incorporated into carbonated hydroxyapatite (CHA) to create Mg, Zn, and CO_3 multi-substituted hydroxyapatite (MgZnCHA). Physicochemical properties were thoroughly characterized using ICP-OES, XRD, FTIR, and FESEM-EDS. The results indicated that the optimal concentrations for Mg and Zn are 1.78-1.997 mole% and 2.94-8.17 mole%, respectively. Notably, a single multi-substituted HA phase was primarily formed at higher Zn concentrations (MgZnCHA6.5%), avoiding the secondary phase (β-TCP) found at lower concentrations. Antimicrobial efficacy was tested using a well-diffusion method, with the best results observed for MgZnCHA containing 1.78 mole% Mg and 6.22 mole% Zn. Cytotoxicity was evaluated *in vitro* using the BJ1 human fibroblast cell line. Multi-doped powders containing 1.997 mole% Mg and 8.17 mole% Zn have significantly improved cell survival. These multi-substituted HA nanopowders hold significant promise for therapeutic applications in bone and dental regeneration.

Keywords: Mg; Zn; CO_3; multi-substituted hydroxyapatite; antimicrobial activity; BJ1 cells.

1. Introduction

Biological apatite is a nonstoichiometric carbonated HA (CHA). The CO_3^{2-} concentration of natural apatite varies from 3 to 8 wt.% [1] according to the anionic substitutions based on the age and species. Young bone has a variable quantity of carbonate group, with a larger content of B-type (the CO_3^{2-} group substitutes the PO_4^{3-} position) compared to the A-type (the CO_3^{2-} group substitutes in the OH^- position) of the apatite crystals [2]. It may contain other ions such as Mg^{2+}, Zn^{2+}, Mn^{2+}, and F^-. During the early phases of osteogenesis, cartilage and natural bone tissue have higher Mg concentrations than mature bone. Human bone typically contains 5.8 and 0.55 wt.% of carbonate and Mg ions, respectively [3], whereas dentin contains an Mg amount of 1.3 wt.% [4].

While synthetic biomimetic apatites have shown promise in enhancing degradation and biological activity [5–11], the optimal incorporation of multiple ions to achieve synergistic benefits in both antimicrobial activity and biocompatibility remains a key challenge. MgO is the most significant cationic substitution, making about 6-7 mole% of the total bone mass. This favors the mechanical and biological features of HA but does not significantly alter its crystallographic characteristics [3]. It promotes osteoblast growth during the initial phases of osteogenesis, acting similarly to a growth factor that stimulates bone formation [12]. Moreover, synthetic magnesium-doped hydroxyapatites are highly resorbable and provide a source of magnesium, which has a detrimental effect on skeletal metabolism and bone fragility [13,14]. Therefore, it can be utilized to treat magnesium deficiency. It has already been demonstrated that bone fillers containing Mg-substituted HA enhance the interaction of cells and form new bone [15,16]. Yet, the substitution of Mg ion in the apatite is limited as greater amounts cause its dissociation to Mg-tri-calcium phosphate. But it can be enhanced by co-substituting CO_3^{2-} ions with Mg ions [15]. Also, Zinc is important to the bone tissue biochemistry and the most prevalent trace metal element identified in bone [17,18]. Hydroxyapatite improves osteoblast cell adhesion, proliferation, and differentiation when combined with zinc ions [19,20]. Moreover, enzymes important for bone metabolism require zinc ions as cofactors. Zinc-doped HA is also well-known for its antibacterial properties against common bone and dental infection-related bacteria and fungi [21–29]. Zn^{2+} ions are released, preventing the infection by fungi. A percent of 3% of zinc may lead to a 72-hour drop in *C. albicans* biofilm [30]; similarly, the cell counts considerably dropped in the dark and at a lower concentration (1%) of Zn^{2+} ion [31]. Moreover, zinc doping inhibits bacterial plaque growth on tooth enamel; on the other hand, it enhances its remineralization. ZnHA (1%) enhanced osteoblast proliferation and their antibacterial properties. On the other hand, ZnHA (2%) reduced biocompatibility at high doses, yet it readily combats the bacteria of enamel (*Streptococcus sobrinus*, *Lactobacillaceae*, and *Streptococcus mutans*).

Most of the recorded studies [23,25,26,30,32] found that HA includes 0.1-4% zinc substitution. Maximum levels of biocompatibility, osteoconductivity, and antibacterial capability are observed when the Zn^{2+} ion content is between 1 and 2% [23,24,27]. It was found that ZnHA, compared with pure HA, hastens the formation of newly formed bone after implantation in rats and rabbits for 1 month and 2 months [33,34]. Despite the individual benefits of Mg and Zn doping, there is a research gap in systematically exploring the synergistic effects of multi-substituting HA with Mg, Zn, and CO_3 ions simultaneously, particularly concerning their combined impact on phase formation, antimicrobial efficacy, and cellular biocompatibility.

Several methods are employed in the production of monovalent- and divalent-doped hydroxyapatite, including microwave hydrothermal synthesis, co-precipitation, solid-state reaction, reversed microemulsion, sol-gel method, and mechanochemical technique [35–37]. The Mg, Zn-containing HA nanoparticles can be prepared using a low-cost, simple wet precipitation approach that incorporates CO3 ions to form multi-substituted hydroxyapatite resembling natural apatite. A thorough study is needed on the apatite phase formed, including the determination of the extent of substitution of Mg, Zn, and CO_3 modified hydroxyapatites, as well as a review of their biocompatibility characteristics based on zinc content.

2. Materials and Methods

2.1. Materials preparation of hydroxyapatite powders.

Hydroxyapatite nanopowders were made using a wet precipitation method [38–40]. Precursors used included: $CaCO_3$ (Merck, 98.5-100.5%), HNO_3 (S.D.Fine-Chem Ltd.), $(NH_4)_2HPO_4$ (Merck, ≥99.0%), $NaHCO_3$ (VWR Chemicals BDH)) and $Mg(NO_3)_2$ x $6H_2O$ and $Zn(NO_3)_2$ x $6H_2O$, both are purchased from Alpha Chemika, 99% and 98 or 96%, respectively; the molar concentrations and ratios are shown in Tables 1 and 2. $Ca(NO_3)_2$ as well as $(NH_4)_2HPO_4$ solution stocks were prepared: estimated proportions from $CaCO_3$ and HNO_3 acid, as well as $(NH_4)_2HPO_4$, were individually dissolved in distilled water. The different additions were added while stirring at room temperature, and a pH of 8.33 was maintained. The mixture was then allowed to digest for 24 h at 40ºC before being aged for another 24 hours at room temperature. Finally, the obtained precipitates were rinsed with distilled water, then centrifuged, and further calcined at 400 and 600ºC.

Table 1. The elemental proportion in moles in the produced powders.

Sample	Constituent mole concentration					Ca/P molar ratio
	Ca	P	Mg	Zn	CO_3	
HA	5	3	---	---	---	1.67
MgZnCHA3%	4.525	2.55	0.325	0.15	0.45	1.77
MgZnCHA5%	4.425	2.55	0.325	0.25	0.45	1.73
MgZnCHA6.5%	4.35	2.55	0.325	0.325	0.45	1.7

Table 2. Molar percentage of the constituents of the prepared powders.

Sample	Mg/(Ca+Mg+Zn) (%)	Zn/(Ca+Mg+Zn) (%)	CO_3/(P+CO_3) (%)
HA	---	---	---
MgZnCHA3%	6.5	3	15
MgZnCHA5%	6.5	5	15
MgZnCHA6.5%	6.5	6.5	15

2.2. Powders characterization.

The produced powders were analyzed by ICP-OES (inductively coupled plasma-optical emission spectrometry) using the Agilent 5100 Synchronous Vertical Dual View (SVDV) model. The values of the substituted ion concentrations were used to calculate the respective calcium-to-phosphorus molar ratios. The phase composition was determined using an XRD Bruker D8 Discover (Germany) at a wavelength of 1.54 Å and radiation operating at 40 kV. The FTIR-ATR Brucker Vertex 80 V equipment was used to determine the different constituting groups in the 400 to 4000 cm^{-1} range. The agglomeration, morphology, and the Ca, P, Mg, and Zn content of the samples were determined with a scanning electron microscope (SEM), the instrument QUANTA EFG 250 scanning electron microscope equipped with energy-dispersive X-ray spectroscopy (EDS). The samples were coated with a thin layer of gold.

2.3. Antimicrobial activity study.

The antimicrobial effect of prepared apatites was evaluated using the pathogenic microorganisms, *Staphylococcus aureus* (ATCC 6538), *Escherichia coli* (ATCC 25922), *Helicobacter pylori* (ATCC 43526), and *Candida albicans* (ATCC 10231). These microorganisms were chosen for their relevance to bone and tooth infections: *S. aureus* and *E.*

coli are common in bone infections, *S. aureus* and *C. albicans* are associated with dental infections [41–43], and *H. pylori* is linked to bone density loss (osteoporosis) rather than direct infections [44].

The microbe "inoculum" with a size of 1.5×10^8 CFU /mL was produced in broth at 37ºC overnight. 100 µL of the material in DMSO (dimethyl sulfoxide) at a 50 mg/mL concentration was placed into each well in each trial. The samples after cooling and solidifying the media were separately placed into 0.9 cm wells of previously prepared infected agar dishes [45]. The plates were refrigerated for 1 hour to promote sample diffusion, then incubated for 24 hours at 37ºC. Zonal inhibition (ZI) was measured and reported in millimeters (mm). DMSO as a blank was tested with different microorganisms under the same conditions. Gentamicin (10 µg, standard antibiotic disc) and Miconazole (10 µg, standard antifungal disc) were used as controls for comparison to evaluate the efficacy of the tested samples against both bacterial and fungal pathogenic strains.

2.4. In vitro biocompatibility study.

To determine cell viability, the yellow 3-(4,5-dimethylthiazol-2-yl)-2,5-diphenyl tetrazolium bromide (MTT) was reduced to formazan, a purple product [46]. The following procedures were all completed in a sterile environment inside a Baker, SG403INT (Sanford, ME, USA) biosafety class II level Laminar flow cabinet. Cells (BJ1 cell line, purchased from ATCC) were in suspension in DMEM-F12 media, 1% antibiotic-antimycotic combination (10000 g/mL streptomycin sulfate, 10000 U/mL potassium penicillin, and 25 µg/mL amphotericin B), and 1% l-glutamine under 5% CO_2 at 37ºC. Cells were grown in 96-well microtiter plastic plates (Sheldon, TC2323, Cornelius, OR, USA) for 10 days before being seeded at a density of 10×10^3 cells per well in fresh complete growth medium. Experiments were conducted in triplicate, with three wells per sample concentration for each independent experiment. Cells were either cultivated alone (negative control) or with samples in concentrations ranging from 0.78 - 100 µg/mL. After 48 hours of incubation, the medium was withdrawn, and an amount of MTT salt (40 µL) was added to each well. The wells were then incubated for an additional 4 h under 5% CO_2 and at 37ºC. 200 µL of 10% SDS (sodium dodecyl sulfate) in de-ionized water was added to each well to stop the reaction and dissolve the formed crystals. A positive control, DOX, was used under the same circumstances, as 100 µg/ml results in 100% mortality [47]. A microplate multi-well reader (Bio-Rad Laboratories Inc., model 3350, Hercules, USA) was used to measure the absorbance at 595 nm with a reference wavelength of 620 nm. Statistical analysis was performed using one-way ANOVA, followed by the Holm Comparison Test and Bonferroni's Multiple Post-Test, with significance set at $p < 0.05$.

3. Results and Discussion

The results obtained by ICP-OES examination of the apatite powders calcined at 400ºC are shown in Table 3. There is a noticeable discrepancy between the calculated dopant ratios (Tables 1 and 2) and the measured dopant ratios for the powders produced in Table 3. Accordingly, not all the amount of the dopants added participated in the structure of the HA. The amount of Mg introduced in the HA lattice was around ~1.78-1.997 mole% out of the calculated value (6.5 mole%). In contrast, the amount of Zn entered in the HA lattice is slightly more or less than the calculated values. This may be attributed to a kind of competition between

the Mg and Zn in partially substituting the Ca^{2+} sites in the HA. Thus, it tends to allow more Zn^{2+} than Mg^{2+} to enter the lattice. Increasing the Zn mole% doping allows a higher percentage of Mg into the HA lattice (MgZnCHA6.5%). Kojima *et al*. [48] reported that the Zn incorporated percentages were identical to those in the feed, while the Mg loading values were only about half as high. This is explained by the variation in the ionic radius values of Mg, which is ~0.66 Å, i.e., less than Zn (~0.74 Å), and Ca (~0.99 Å) ions. It's probable that only minuscule amounts of Mg replaced Ca ions in the structure of the HA crystal [48].

Table 3. Elemental composition of different powders calcined at 400ºC measured by ICP-OES.

Sample	Mg/(Ca+Mg+Zn) (%)	Zn/(Ca+Mg+Zn) (%)	(Ca+Mg+Zn)/P Molar ratio	Ca/P Molar ratio
HA	---	---	1.58	1.58
MgZnCHA3%	1.81	2.94	1.69	1.61
MgZnCHA5%	1.78	6.22	1.53	1.41
MgZnCHA6.5%	1.997	8.17	1.65	1.48

The XRD patterns in Figure 1 are of pure and ion-substituted HA nanopowders. They correspond to the primary peaks of the HA as specified by the ICDD standard (JCPDS 09-432). Simultaneous doping of Mg and Zn in the HA lattice showed the presence of β-TCP in the calcined samples, whereas at a higher Zn doping percentage (about 8.17 mole%), hydroxyapatite was the phase predominantly formed. This means that, in the presence of Mg, the Zn occupied most of the Ca sites, avoiding the decomposition of HA when calcined at 400 and 600ºC. Moreover, the intensities of the XRD peaks decreased with increasing Zn mole%. The characteristic peaks of MgZnCHA6.5% became broader. The introduction of Mg^{2+} with Zn^{2+} caused a reduction in the crystallite size of HA. This might indicate a degree of distortion of the crystal structure somewhat accompanying the variation in the smaller Mg^{2+} and Zn^{2+} ionic radii compared to the Ca^{2+} ionic radius [49].

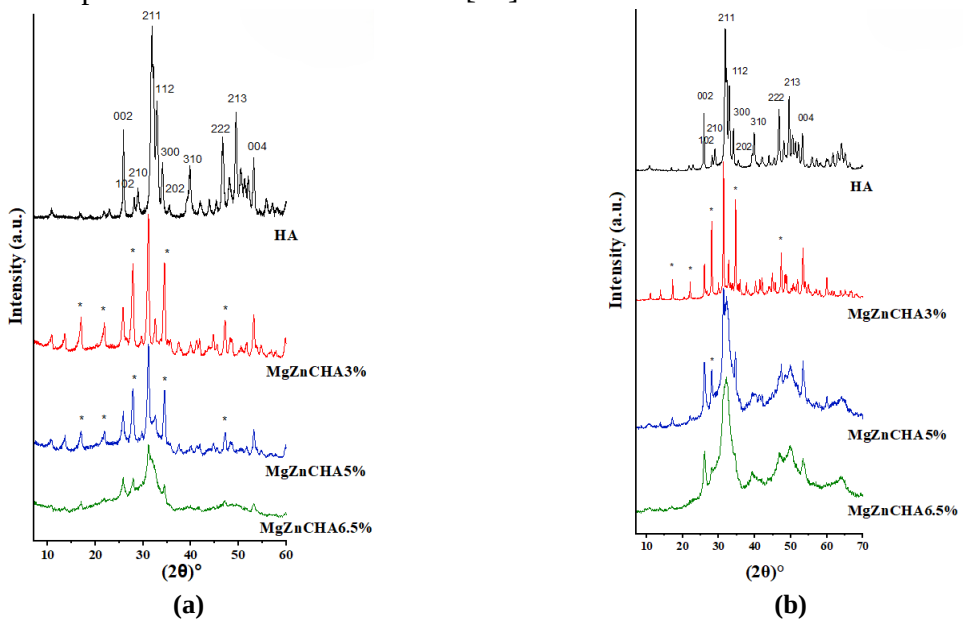

Figure 1. XRD patterns of produced powders that had been calcined at **(a)** 400ºC; **(b)** 600ºC, showing dominant HA phases (JCPDS 09-432) and β-TCP formation (*) at specific compositions.

Apart of the previously reported FTIR spectra [39], (Figure 2), The prepared apatite powders displayed the typical absorption bands associated with the phosphate (ν_2 bending at ~473 cm^{-1}; ν_4 bending at ~562 cm^{-1} and ~600 cm^{-1}; ν_1 symmetric stretch at ~962 cm^{-1}; ν_3 asymmetric stretch at ~1024-1090 cm^{-1}) and hydroxyl (vibrational at ~630 cm−1; stretch at

~3571 cm^{-1}) modes. Depending on their concentration, particularly in the substituted HA, the substitution of CO_3 in the HA lattice changed the appearance and/or existence of specific phosphate bands. Phosphate bands at 562 and 962 cm^{-1} moved to ~552 and 953 cm^{-1} in MgZnCHA3% and MgZnCHA5%, respectively. While the band at 962 cm−1 diminished in the higher Zn substituted one (MgZnCHA6.5%). Whereas the band at ~1090 cm^{-1} disappeared in all substituted HA. Both the hydroxyl bands at ~630 and 3571 cm^{-1} diminished or disappeared in all substituted HA, confirming that the dopants occupied the CO_3 and the OH site beside the PO_4 site, or otherwise the β-TCP is formed. An additional symmetric stretching band of PO_4 of β-TCP at ~1003 cm^{-1} [50] was observed in the spectra of MgZnCHA3%, indicating the β-TCP formation in high percentage, beside the HPO_4 band at 990 cm^{-1} [50]. The produced powders' spectra showed bands (ν_2 bending, ~877 cm^{-1}; ν_3 stretching, ~1410 and 1444 cm^{-1}) linked to carbonate in the B position [51]. Comparing the substituted HA powders to the pure phase, the carbonate bands in the substituted HA powders, especially in MgZnCHA6.5%, were more pronounced. The spectra of HA showed a short band at 1550 cm^{-1} that indicated A-carbonation at the hydroxyl site as well. As a result, these powders were primarily classified as B-carbonated types. The water bands were observed at 1640 cm^{-1} and at 3000-3700 cm^{-1} [51,52]. ZnO bands, found at 406-430 cm^{-1} in all the Zn-containing HA, are the result of the tetrahedral ZnO_4 and ZnO bonded to phosphate groups [53].

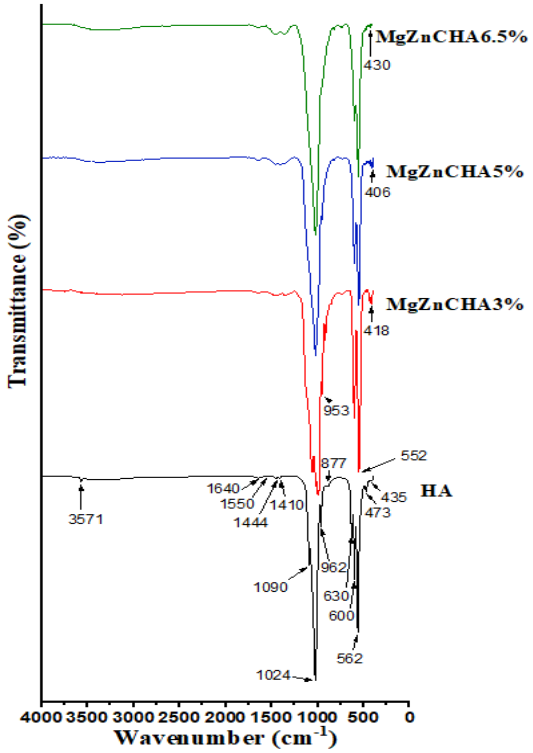

Figure 2. FTIR Spectra of lyophilized powders: HA, MgZnCHA3%, MgZnCHA5%, MgZnCHA6.5%.

There is an ongoing debate over how much Mg can replace Ca. Magnesium has been reported to be able to replace calcium in the full spectrum of compositions by Patel *et al* (1980) [54]. According to Bigi *et al*. [55], the HA crystal structure at most contained magnesium amounts of around 7 at.%. According to Fadeev *et al*. [56] and Fuzeng *et al*. [57], the addition of 5 at.% Mg^{2+} caused a whitlockite and a tiny particle, defect-rich HA to develop.

The obtained results showed that magnesium could be introduced in a very limited percentage (1.997 mole%) in the HA structure after increasing the amount of Zn

(MgZnCHA6.5%), which allowed the highest percentage of both Mg and Zn doping on the HA, and that avoiding the formation of secondary phase after calcination at 400 and 600ºC.

The FESEM images at 30.00 KX magnification revealed that the hydroxyapatite powders are made of clusters of tiny, non-uniform particles (Figure 3). Additionally, upon ion doping, more microscale aggregates were observed. This is likely due to ion exchange within the material, leading to coarsening of crystallite size and the formation of denser microscale aggregates. The proportions of Ca, P, Mg, and Zn determined by EDS in MgZnCHA agglomerates are in good agreement with the ICP-OES results (Table 3).

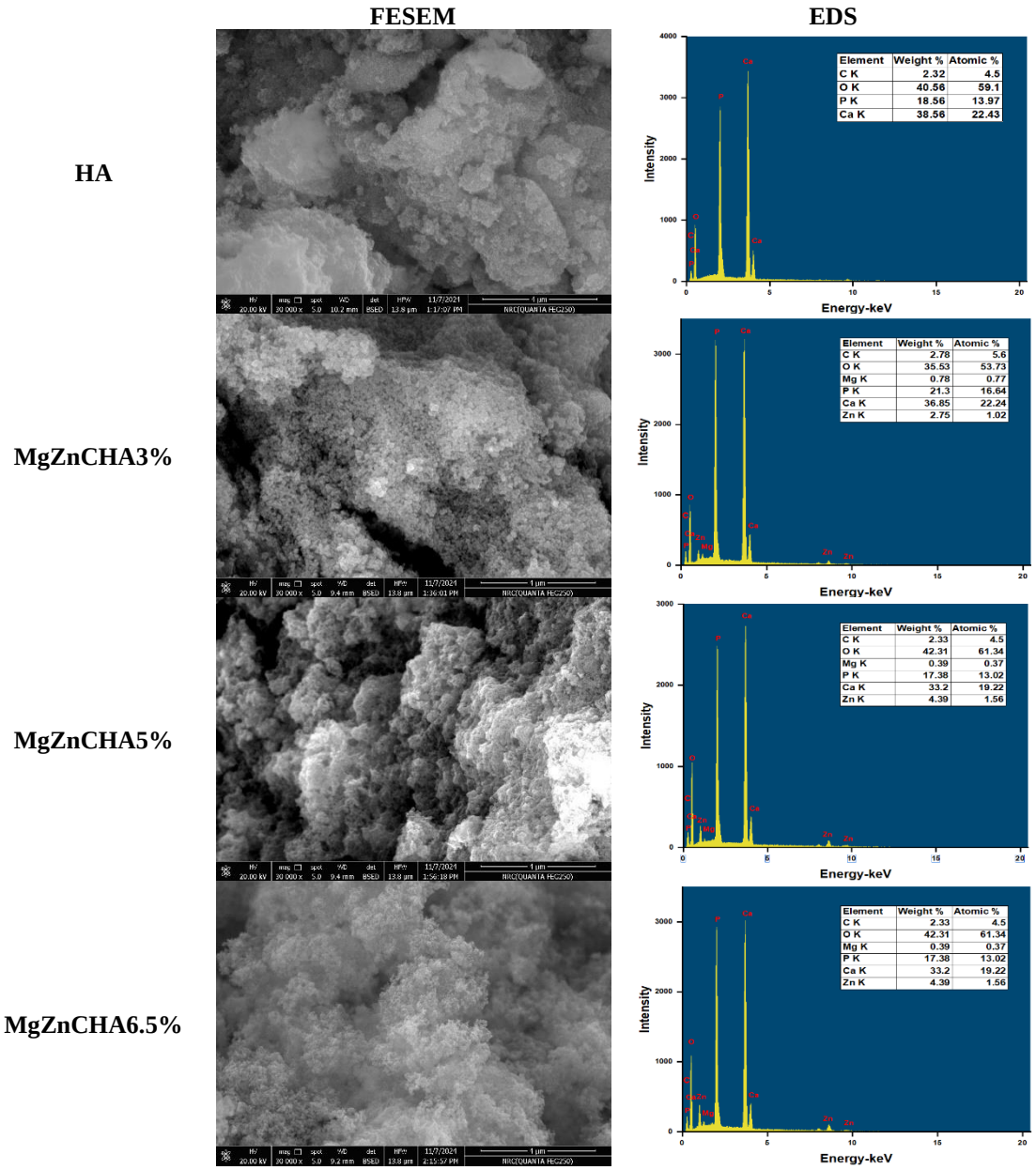

Figure 3. FESEM images of powders calcined at 400ºC: HA, MgZnCHA3%, MgZnCHA5%, MgZnCHA6.5%, at the magnification of 30.00 KX. EDS analysis for powders showed their elemental composition.

The antimicrobial efficacy of calcined powder samples at 400ºC was tested against four microbes. The measured zones of inhibition are shown in Table 4. The inhibitory impact of the samples was compared based on these results. All apatite samples were more effective against Candida albicans compared to the control. MgZnCHA5% showed the highest effectiveness of the apatite sample against all tested bacterium species, *Staphylococcus aureus*, *Escherichia coli*, and *Helicobacter pylori* (Figure 4). At the same time, MgZnCHA6.5% was less effective.

Moreover, the microstructure and variations in crystal structure resulting from secondary phases formed at calcination temperatures had a significant impact on the antibacterial activity [58]. MgZnCHA6.5% sample exhibited almost pure phase of HA, while MgZnCHA5% exhibited mixed β-TCP and HA phases. Among the tested apatite powders, MgZnCHA5% has the highest antibacterial effect against all microbes. This is explained by the reason that MgZnCHA5% has a high Zn^{2+} concentration (6.22 mole%) and also contains β-TCP, which contributes to the solubility and bioresorbability of Mg^{2+}, Zn^{2+}, and CO_3^{2-} and leads to enhanced antibacterial activity [59,60]. The increased solubility is caused by the low negative logarithm of the solubility product of β-TCP (pKsp = 28.90) in comparison to that of HA (pKsp = 116.80) [61]. This multi-doping strategy with specific ion ratios and mixed phases appears more effective than systems incorporating single dopants, such as Sr- or Ag-doped HA, which primarily rely on ion release for antimicrobial effects but may lack the synergistic benefits observed here with complex compositions and phase mixtures [6,27]. Future studies should explore the incorporation of copper into Mg-substituted HA systems, leveraging Cu^{2+}'s potent antimicrobial properties to develop next-generation multi-ion platforms with enhanced infection control and osteogenic functionality.

Table 4. Inhibition zone diameter (mm) of calcined powders (HA, MgZnCHA3%, MgZnCHA5%, and MgZnCHA6.5%) against different pathogenic strains.

Sample	Inhibition zone diameter (mm)			
	Staphylococcus aureus	***Escherichia coli***	***Helicobacter pylori***	***Candida albicans***
HA	15	16	13	17
MgZnCHA3%	17	17	12	16
MgZnCHA5%	16	20	15	19
MgZnCHA6.5%	15	13	14	16
CN	21	14	21	---
MIZ	---	---	---	14
DMSO	nz	nz	nz	nz

CN= Gentamicin (10 µg, disc), MIZ= Miconazole (10 µg, disc), and DMSO= dimethyl sulfoxide. nz= no recorded zone.

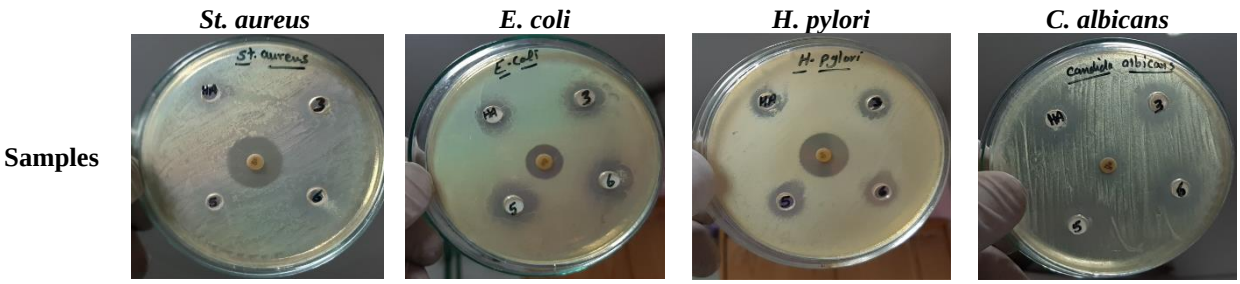

Figure 4. Images of the antimicrobial effects of apatite samples that were calcined at 400ºC on different microbes after 24 h of incubation. HA, **(3)** MgZnCHA3%, **(5)** MgZnCHA3%, **(6)** MgZnCHA6.5%, the positive control is located in the center.

Cell viability tests were conducted on calcined powders at 400ºC using the BJ1 fibroblast cell line after 48 hours of incubation. The negative control (cells cultivated alone) exhibited 0% cytotoxicity. The MTT assay indicated that Mg, Zn, and CO_3 multi-substituted hydroxyapatite, MgZnCHA6.5% (with measured Zn=8.17 mole%), decreased the cytotoxicity on BJ1 cells as compared to pure HA ($p<0.05$) (Figure 5). This may be due to the high Zn release besides the Mg. The presence of Zn, Mg, and CO_3 is advantageous for cellular metabolism. The particle size has a significant impact on cytotoxicity. The particle size reduced as the concentration of Zn^{2+} ions in HA increased to 8.17 mole%, as seen by the broadening of XRD peaks in Figure 1. The percentage of live cells was greater with measured 6.22 mole%

Zn containing HA nanoparticles than with cells cultivated with measured 2.94 mole% Zn containing HA nanoparticles under the same conditions. The MgZnZnCHAHA3%, containing β-TCP in high percentage, showed the highest cytotoxicity percentage (A significant difference ($p<0.01$) was detected between MgZnZnCHAHA3% and all other samples), in contrast to MgZnCHA6.5%, which is mostly HA phase with multi-ionic substitution. Natesan *et al*. have previously reported that tri-calcium phosphate is more toxic than HA [49].

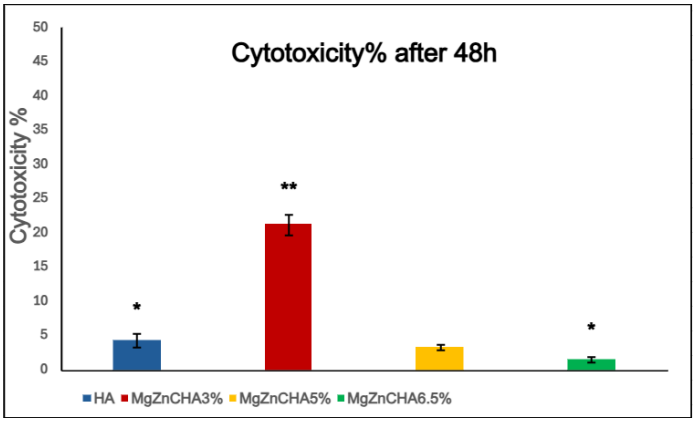

Figure 5. MTT assay showing the percentage of cytotoxicity of the powders that were calcined at 400ºC after being incubated with the BJ1 cell line for 48 hours at a concentration of 100 µg/mL. * $p<0.05$, ** $p<0.01$.

4. Conclusions

In summary, Mg, Zn, and CO_3 multi-substituted HA nanopowders were successfully synthesized via a cost-effective wet precipitation method. Characterization techniques confirmed the successful, albeit limited, substitution of Ca by Mg (approx. 1.78-1.997 mole%) and Zn (approx. 2.94-8.17 mole%) within the HA structure. While lower Zn concentrations resulted in mixed phases, increasing the Zn content led to the formation of a predominantly multi-substituted HA phase with higher Mg and Zn incorporation, minimizing secondary products and exhibiting reduced crystallinity. The presence of B-type CO_3-doping further enhances the biomimetic nature and solubility of the synthetic apatite at physiological pH [62]. Optimal antimicrobial activity was achieved with MgZnCHA containing 1.78 mole% Mg and 6.22 mole% Zn, demonstrating superior efficacy against common pathogenic strains relevant to bone and dental infections. Furthermore, the unique physicochemical properties of the doped powders significantly enhanced the viability of BJ1 fibroblast cells, particularly with the (1.997 mole% Mg + 8.17 mole% Zn) multi-substituted apatite powder, indicating improved biocompatibility.

The manufactured nanopowders have been useful to the sector, and their optimal composition was developed to deliver a distinctive multi-doped hydroxyapatite phase with very high purity or TCP. These biomaterials may be appropriate for biomedical applications, such as implanting or coating metallic implants for tooth and bone regeneration. However, future work should investigate the long-term *in vivo* performance and degradation kinetics of these materials. Additionally, exploring the scalability of this wet precipitation synthesis method for large-scale production would be a critical next step towards clinical translation.

Author Contributions

SK: visualization, data curation, writing - original draft; HA: methodology, formal analysis, resources; HE: methodology, formal analysis, resources; DI: conceptualization, research administration, resources, supervision, writing - review & editing. All authors approved the final version of the manuscript.

Institutional Review Board Statement

Not applicable.

Informed Consent Statement

Not applicable.

Data Availability Statement

Data supporting the findings of this study are available upon reasonable request from the corresponding author.

Funding

This research received no external funding.

Acknowledgments

We acknowledge the support of the National Research Center, Egypt, Refractories, Ceramics, and Building Materials Department, for providing the laboratory infrastructure.

Conflicts of Interest

The authors declare no conflict of interest.

References

1. De Groot, K. Bioceramics calcium phosphate; CRC Press: Boca Raton, FL, USA, **2018**.
2. Rey, C.; Renugopalakrishnan, V.; Collins, B.; Glimcher, M. Fourier transform infrared spectroscopic study of the carbonate ions in bone mineral during aging. *Calcif. Tissue. Int.* **1991**, *49*, 251–258, https://doi.org/10.1007/bf02556214.
3. LeGeros, R.Z. Calcium Phosphates in Oral Biology and Medicine. Karger: **1991**; Volume 15, https://doi.org/10.1159/isbn.978-3-318-04021-0.
4. Landi, E.; Uggeri, J.; Medri, V.; Guizzardi, S. Sr, Mg cosubstituted HA porous macro-granules: potentialities as resorbable bone filler with antiosteoporotic functions. *J. Biomed. Mater. Res. A* **2013**, *101*, 2481–2490, https://doi.org/10.1002/jbm.a.34553.
5. Kubiak-Mihkelsoo, Z.; Kostrzębska, A.; Błaszczyszyn, A.; Pitułaj, A.; Dominiak, M.; Gedrange, T.; Nawrot-Hadzik, I.; Matys, J.; Hadzik, J. Ionic doping of hydroxyapatite for bone regeneration: Advances in structure and properties over two decades—a narrative review. *Appl. Sci.* **2025**, *15*, 1108, https://doi.org/10.3390/app15031108.
6. Murugesan, V.; Murugeasan, A.; Ganesan, S.; Murugesan, S.; Dixit, S.; Vaiyapuri, M. Fabrication and characterization of hydroxyapatite substituted with Mg^{2+}, Sr^{2+}, and ampicillin for bone and antibacterial applications. *Mater. Sci. Eng. B* **2025**, *316*, 118131, https://doi.org/10.1016/j.mseb.2025.118131.
7. 1. Siri-Udom, S.; Prasitnok, O.; Prasitnok, K.; Khemthong, P.; Phawa, C.; Roschat, W.; Utara, S.; Prachumrak, N.; Sripirom, J.; Phatai, P. Synthesis, Characterization, and Functional Analysis of Mixed Manganese/Cerium Oxide/Hydroxyapatite Nanocomposites for Antibacterial Applications. *J. Clust. Sci.* **2025**, *36*, 28, https://doi.org/10.1007/s10876-024-02750-6.

8. Hassanain, M.; Abdel-Ghafar, H.M.; Hamouda, H.I.; El-Hosiny, F.I.; Ewais, E.M. Enhanced antimicrobial efficacy of hydroxyapatite-based composites for healthcare applications. *Sci. Rep.* **2024**, *14*, 26426, https://doi.org/10.1038/s41598-024-76088-4.
9. Ghabour, O.; Taha, N.; Aboul Gheit, S.; Mohy El Din, M. Evaluation of magnesium-based scaffolds fabricated using a modified sintering technique and two types of space holding agents (*in vitro* study). *BDJ open* **2025**, *11*, 20, https://doi.org/10.1038/s41405-025-00299-8.
10. Shanmugavadivu, A.; Lekhavadhani, S.; Babu, S.; Suresh, N.; Selvamurugan, N. Magnesium-incorporated biocomposite scaffolds: a novel frontier in bone tissue engineering. *J. Magnes. Alloy.* **2024**, *12*, 2231–2248, http://dx.doi.org/10.1016/j.jma.2024.06.001.
11. Daood, U.; Fawzy, A. Development of a bioactive dentin adhesive resin modified with magnesium-doped synthetic hydroxyapatite crystals. *J. Mech. Behav. Biomed. Mater.* **2023**, *140*, 105737, https://doi.org/10.1016/j.jmbbm.2023.105737.
12. Cacciotti, I.; Bianco, A.; Lombardi, M.; Montanaro, L. Mg-substituted hydroxyapatite nanopowders, synthesis, thermal stability and sintering behavior. *J. Eur. Ceram. Soc.* **2009**, *29*, 2969–2978, http://dx.doi.org/10.1016/j.jeurceramsoc.2009.04.038.
13. Rude, R.K.; Singer, F.R.; Gruber, H.E. Skeletal and hormonal effects of magnesium deficiency. *J. Am. College Nutr.* **2009**, *28*, 131–141, https://doi.org/10.1080/07315724.2009.10719764.
14. Sankova, M.V.; Nikolenko, V.N.; Oganesyan, M.V.; Sankov, S.V.; Sinelnikov, M.Y.; Suslov, A.V.; Trishina, A.S.; Zharikova, T.S.; Pontes-Silva, A.; Zharikov, Y.O. Magnesium deficiency and its interaction with the musculoskeletal system, exercise, and connective tissue: An evidence synthesis. *Sport Sci. Health* **2024**, *20*, 715-726, https://doi.org/10.1007/s11332-024-01179-8.
15. Landi, E.; Tampieri, A.; Mattioli-Belmonte, M.; Celotti, G.; Sandri, M.; Gigante, A.; Fava, P.; Biagini, G. Biomimetic Mg-and Mg, CO3-substituted hydroxyapatites: synthesis characterization and *in vitro* behaviour. *J. Eur. Ceram. Soc.* **2006**, *26*, 2593-2601, https://doi.org/10.1016/j.jeurceramsoc.2005.06.040.
16. Landi, E.; Logroscino, G.; Proietti, L.; Tampieri, A.; Sandri, M.; Sprio, S. Biomimetic Mg substituted hydroxyapatite: from synthesis to *in vivo* behavior. *J. Mater. Sci. Mater. Med.* **2008**, *19*, 239–247, https://doi.org/10.1007/s10856-006-0032-y.
17. Yamaguchi, M.; Oishi, H.; Suketa, Y. Stimulatory effect of zinc on bone formation in tissue culture. *Biochem. Pharmacol.* **1987**, *36*, 4007–4012, https://doi.org/10.1016/0006-2952(87)90471-0.
18. 1. Thian, E.; Konishi, T.; Kawanobe, Y.; Lim, P.; Choong, C.; Ho, B.; Aizawa, M. Zinc-substituted hydroxyapatite: a biomaterial with enhanced bioactivity and antibacterial properties. *J. Mater. Sci.: Mater. Med.* **2013**, *24*, 437-445, https://doi.org/10.1007/s10856-012-4817-x.
19. Cox, S.C.; Jamshidi, P.; Grover, L.M.; Mallick, K.K. Preparation and characterisation of nanophase Sr, Mg, and Zn substituted hydroxyapatite by aqueous precipitation. *Mater. Sci. Eng. C Mater. Biol. Appl.* **2014**, *35*, 106–114, https://doi.org/10.1016/j.msec.2013.10.015.
20. Dornelas, J.; Dornelas, G.; Rossi, A.; Piattelli, A.; Di Pietro, N.; Romasco, T.; Mourão, C.F.; Alves, G.G. The incorporation of zinc into hydroxyapatite and its influence on the cellular response to biomaterials: a systematic review. *J. Funct. Biomater.* **2024**, *15*, 178, https://doi.org/10.3390/jfb15070178.
21. Predoi, D.; Iconaru, S.L.; Deniaud, A.; Chevallet, M.; Michaud-Soret, I.; Buton, N.; Prodan, A.M. Textural, structural and biological evaluation of hydroxyapatite doped with zinc at low concentrations. *Materials* **2017**, *10*, 229, https://doi.org/10.3390/ma10030229.
22. El Hotaby, W.; Bakr, A.; Sherif, H.; Soliman, A.A.; Hemdan, B. Exploring the antimicrobial and anticancer activities of zinc doped nanohydroxyapatite prepared via ultrasonic-assisted method for bone tissue engineering. *J. Mater. Res.* **2024**, *39*, 1911-1925, https://doi.org/10.1557/s43578-024-01350-4.
23. Chung, R.J.; Hsieh, M.F.; Huang, K.C.; Perng, L.H.; Chou, F.I.; Chin, T.S. Anti-microbial hydroxyapatite particles synthesized by a sol-gel route. *J. Sol-Gel Sci. Technol.* **2005**, *33*, 229–239, https://doi.org/10.1007/s10971-005-5618-1.
24. Li, Y.; Shi, X.; Li, W. Zinc-containing hydroxyapatite enhances cold-light-activated tooth bleaching treatment *in vitro*. *BioMed. Res. Int.* **2017**, *2017*, 6261248, https://doi.org/10.1155/2017/6261248.
25. Anwar, A.; Akbar, S.; Sadiqa, A.; Kazmi, M. Novel continuous flow synthesis, characterization and antibacterial studies of nanoscale zinc substituted hydroxyapatite bioceramics. *Inorg. Chim. Acta*. **2016**, *453*, 16–22, http://dx.doi.org/10.1016/j.ica.2016.07.041.
26. Ohtsu, N.; Kakuchi, Y.; Ohtsuki, T. Antibacterial effect of zinc oxide/hydroxyapatite coatings prepared by chemical solution deposition. *Appl. Surf. Sci.* **2018**, *445*, 596–600, https://doi.org/10.1016/j.apsusc.2017.09.101.

27. Ueno, M.; Miyamoto, H.; Tsukamoto, M.; Eto, S.; Noda, I.; Shobuike, T.; Kobatake, T.; Sonohata, M.; Mawatari, M. Silver-containing hydroxyapatite coating reduces biofilm formation by methicillin-resistant Staphylococcus aureus *in vitro* and in vivo. *BioMed Res. Int.* **2016**, *2016*, 8070597, https://doi.org/10.1155/2016/8070597.
28. Cuypers, L.A.; de Boer, L.; Wang, R.; Walboomers, X.F.; Yang, F.; Zaat, S.A.; Leeuwenburgh, S.C. Antibacterial activity of zinc-doped hydroxyapatite and vancomycin-loaded gelatin nanoparticles against intracellular staphylococcus aureus in human thp-1 derived macrophages. *ACS Appl. Nano Mater.* **2024**, *7*, 21964-21974, https://doi.org/10.1021/acsanm.4c03941.
29. Helbig, K.; Bleuel, C.; Krauss, G.J.; Nies, D.H. Glutathione and transition-metal homeostasis in Escherichia coli. *J. Bacteriol.* **2008**, *190*, 5431–5438, https://doi.org/10.1128/jb.00271-08.
30. Groza, A.; Ciobanu, C.S.; Popa, C.L.; Iconaru, S.L.; Chapon, P.; Luculescu, C.; Ganciu, M.; Predoi, D. Structural properties and antifungal activity against Candida albicans biofilm of different composite layers based on Ag/Zn doped hydroxyapatite-polydimethylsiloxanes. *Polymers* **2016**, *8*, 131, https://doi.org/10.3390/polym8040131.
31. Iconaru, S.L.; Prodan, A.M.; Buton, N.; Predoi, D. Structural characterization and antifungal studies of zinc-doped hydroxyapatite coatings. *Molecules* **2017**, *22*, 604, https://doi.org/10.3390/molecules22040604.
32. Samani, S.; Hossainalipour, S. M.; Tamizifar, M; Rezaie, H. R. *In vitro* antibacterial evaluation of sol-gel-derived Zn-, Ag-, and (Zn+Ag)-doped hydroxyapatite coatings against methicillin-resistant Staphylococcus aureus. *J. Biomed. Mater. Res. Part A.* **2013**, *101*, 222–230, https://doi.org/10.1002/jbm.a.34322.
33. Yang, H.; Qu, X.; Lin, W.; Wang, C.; Zhu, D.; Dai, K.; Zheng, Y. *In vitro* and in vivo studies on zinc-hydroxyapatite composites as novel biodegradable metal matrix composite for orthopedic applications. *Acta Biomaterialia* **2018**, *71*, 200-214, https://doi.org/10.1016/j.actbio.2018.03.007.
34. Begam, H.; Nandi, S. K.; Chanda, A.; Kundu, B. Effect of bone morphogenetic protein on Zn-HAp and Zn-HAp/collagen composite: a systematic *in vivo* study. *Res. Vet. Sci.* **2017**, *115*, 1–9, https://doi.org/10.1016/j.rvsc.2017.01.012.
35. Sebastiammal, S.; Fathima, A.S.L.; Al-Ghanim, K.A.; Nicoletti, M.; Baskar, G.; Iyyappan, J.; Govindarajan, M. Synthesis and characterisation of magnesium-wrapped hydroxyapatite nanomaterials for biomedical applications. *Surfaces Interfaces* **2024**, *44*, 103779, https://doi.org/10.1016/j.surfin.2023.103779.
36. Bulina, N. V.; Makarova, S. V.; Prosanov, I. Y.; Vinokurova, O. B.; Lyakhov, N. Z. Structure and thermal stability of fluorhydroxyapatite and fluorapatite obtained by mechanochemical method. *J. Solid State Chem.* **2020**, *282*, 121076, http://dx.doi.org/10.1016/j.jssc.2019.121076.
37. Anandan, D.; Jaiswal, A. K. Synthesis methods of hydroxyapatite and biomedical applications: an updated review. *J. Aust. Ceram. Soc.* **2024**, *60*, 663–679, http://dx.doi.org/10.1007/s41779-023-00943-2.
38. Jarcho, M.; Bolen, C. H.; Thomas, M. B.; Bobick, J; Kay, J. F.; Doremus, R. H. Hydroxylapatite synthesis and characterization in dense polycrystalline form. *J. Mater. Sci.* **1976**, *11*, 2027–2035, https://doi.org/10.1007/BF02403350.
39. Korowash, S.I.; Abo-Almaged, H.H.; Ibrahim, D.M. Comparative study of certain substituted ions in hydroxyapatite: characterization and effect on cell viability. *Adv. Nat. Sci.: Nanosci. Nanotechnol.* **2022**, *13*, 025005, https://doi.org/10.1088/2043-6262/ac70d6/meta.
40. Korowash, S. I.; Keskin-Erdogan, Z.; Hemdan, B. A.; Barrios Silva, L. V.; Ibrahim, D. M.; Chau, D. Y. Selenium- and/or copper-substituted hydroxyapatite: a bioceramic substrate for biomedical applications. *J. Biomater. Appl.* **2023**, *38*, 351-360, https://doi.org/10.1177/08853282231198726.
41. Masters, E.A.; Ricciardi, B.F.; Bentley, K.L.d.M.; Moriarty, T.F.; Schwarz, E.M.; Muthukrishnan, G. Skeletal infections: microbial pathogenesis, immunity and clinical management. *Nat. Rev. Microbiol.* **2022**, *20*, 385-400, https://doi.org/10.1038/s41579-022-00686-0.
42. Al-Akwa, A.A.Y.; Zabara, A.Q.M.Q.; Al-Shamahy, H.A.; Al-labani, M.A.; Al-Ghaffari, K.M.; Al-Mortada, A.M.; Al-Haddad, A.M.; Al-Sharani, A.A. Prevalence of Staphylococcus aureus in dental infections and the occurrence of MRSA in isolates. *Univers. J. Pharm. Res.* **2020**, *5*, 23-27, https://doi.org/10.22270/ujpr.v5i2.384.
43. Yoo, Y.J.; Kim, A.R.; Perinpanayagam, H.; Han, S.H.; Kum, K.Y. *Candida albicans* virulence factors and pathogenicity for endodontic infections. *Microorganisms* **2020**, *8*, 1300, https://doi.org/10.3390/microorganisms8091300.
44. Zhang, L.; Zhang, D.; Wei, L.; Zhou, Y.; Li, X.; Chen, R.; Zhang, X.; Chen, S.; Bai, F. H. pylori infection and osteoporosis: a large-scale observational and mendelian randomization study. *BMC Infect. Dis.* **2024**, *24*, 305, https://doi.org/10.1186/s12879-024-09196-1.

45. El-Anssary, A.A.; Abdel Raoof, G.F.; Saleh, D.O.; El-Masry, H.M. Bioactivities, physicochemical parameters and GC/MS profiling of the fixed oil of Cucumis melo L seeds: a focus on anti-inflammatory, immunomodulatory, and antimicrobial activities. *J. Herbmed. Pharmacol* **2021**, *10*, 476–485, http://dx.doi.org/10.34172/jhp.2021.55.
46. Mosmann, T. Rapid colorimetric assays for cellular growth and survival: application to proliferation and cytotoxicity assays. *J. Immunol. Methods.* **1983**, *65*, 55–63, https://doi.org/10.1016/0022-1759(83)90303-4.
47. Thabrew, M.I.; Hughes, R.D.; McFarlane, I.G. Screening of hepatoprotective plant components using a HepG2 cell cytotoxicity assay. *J. Pharm. Pharmacol.* **1997**, *49*, 1132–1135, https://doi.org/10.1111/j.2042-7158.1997.tb06055.x.
48. Kojima, C.; Watanabe, K.; Murata, H.; Nishio, Y.; Makiura, R.; Matsunaga, K.; Nakahira, A. Controlled release of DNA from zinc and magnesium ion-doped hydroxyapatites. *Res. Chem. Intermed.* **2019**, *45*, 23-32, https://doi.org/10.1007/s11164-018-3626-3.
49. Natesan, K.; Shah, W.; Le, H. R.; Tredwin, C. A critical comparison on biocompatibility of different phases of sol-gel derived calcium phosphates as bone graft materials. *J. Biomater. Tissue Eng.* **2015**, *5*, 655–664, https://doi.org/10.1166/jbt.2015.1364.
50. Ibrahim, D.M.; Mostafa, A.A.; Korowash, S.I. Chemical characterization of some substituted hydroxyapatites. *Chem. Centr. J.* **2011**, *5*, 74, https://doi.org/10.1186/1752-153X-5-74.
51. Suchanek, W. L.; Shuk, P.; Byrappa, K.; Rimana, R. E.; TenHuisen, K. S.; Janas, V. F. Mechanochemical-hydrothermal synthesis of carbonated apatite powders at room temperature. *Biomaterials* **2002**, *23*, 699−710, https://doi.org/10.1016/s0142-9612(01)00158-2.
52. Tadic, D.; Peters, F.; Epple, M. Continuous synthesis of amorphous carbonated apatites. *Biomaterials* **2002**, *23*, 2553−2559, https://doi.org/10.1016/s0142-9612(01)00390-8.
53. Moldovan, M.; Prodan, D.; Popescu, V.; Prejmerean, C.; Saroși, C.; Saplonţai, M.; Țălu, S.; Vasile, E. Structural and morphological properties of HA-ZnO powders prepared for biomaterials. *Open Chem.* **2015**, *13*, 000010151520150083, https://doi.org/10.1515/chem-2015-0083.
54. Patel, P.N. Mangnesium calcium hydroxylapatite solid solutions: preparation, IR and lattice constant measurements. *J. Inorg. Nucl. Chem.* **1980**, *42*, 1129−1132, https://doi.org/10.1016/0022-1902(80)80422-2.
55. Bigi, A.; Falini, G.; Foresti, E.; Ripamonti, A. Magnesium influence on hydroxyapatite crystallization. *J Inorg Biochem* **1993**, *49*, 69−78, https://doi.org/10.1016/0162-0134(93)80049-F.
56. Fadeev, I.V.; Shvorneva, L.I.; Barinov, S.M.; Orlovskii, V.P. Synthesis and structure of magnesium-substituted hydroxyapatite. *Inorg. Mater.* **2003**, *39*, 947−950, https://doi.org/10.1023/A:1025509305805.
57. Fuzeng, R. Synthesis and characterization of nanocrystalline Zn, Mg substituted hydroxyapatite. Master's Thesis, Hong Kong University of Science and Technology, Hong Kong, China, **2008**.
58. Phatai, P.; Futalan, C. M.; Kamonwannasit, S.; Khemthong, P. Structural characterization and antibacterial activity of hydroxyapatite synthesized via sol-gel method using glutinous rice as a template. *J. Sol-Gel Sci. Technol.* **2019**, *89*, 764–775, https://doi.org/10.1007/s10971-018-4910-9.
59. Gopi, D.;. Bhuvaneshwari, N.; Indira, J.; Kanimozhi, K.; Kavitha, L. A novel green template assisted synthesis of hydroxyapatite nanorods and their spectral characterization. *Spectrochim. Acta A: Mol. Biomol. Spectrosc.* **2013**, *107*, 196–202, https://doi.org/10.1016/j.saa.2013.01.052.
60. Gokcekaya, O.; Ueda, K.; Ogasawara, K.; Kanetaka, H.; Narushima, T. *In vitro* evaluation of Ag-containing calcium phosphates: effectiveness of Ag-incorporated β-tricalcium phosphate. *Mater. Sci. Eng. C.* **2017**, *75*, 926–933, https://doi.org/10.1016/j.msec.2017.02.059.
61. Jamil, M.; Abida, F.; Hatim, Z.; Elassfouri, M.; Gourri, E. Effects of ions traces on the dissolution of bioceramics composed of hydroxyapatite and β-tricalcium phosphate. *Med. J. Chem.* **2015**, *4*, 51–58.
62. Pan, H.; Darvell, B.W. Effect of carbonate on hydroxyapatite solubility. *Cryst. Growth Des.* **2010**, *10*, 845–850, https://doi.org/10.1021/cg901199h.

Publisher's Note & Disclaimer